Materials & Design 221 (2022) 110914

Contents lists available at ScienceDirect

Materials & Design

journal homepage: www.elsevier.com/locate/matdes

Integration of optical fibre sensors by material extrusion 3-D printing – The effect of bottom interlayer thickness

Shaoquan Wang *, Kaspar Lasn

Department of Mechanical and Industrial Engineering, Norwegian University of Science and Technology (NTNU), Richard Birkelands vei 2B, 7491 Trondheim, Norway

HIGHLIGHTS

- A novel 3-D printing based solution for integrating optical fiber sensors into thermoplastic composite structures is proposed.
- A critical variable in this fiber attachment process (and for surface bonding in general) is the bottom interlayer thickness, which was in-situ investigated for the first time.
- Experimentally measured strain transfer coefficients along the optical fiber sensors remained constant under creep loading.
- A simple calculation method that enables to predict the shear lag effect for optical fibre sensors was derived and validated.

GRAPHICAL ABSTRACT

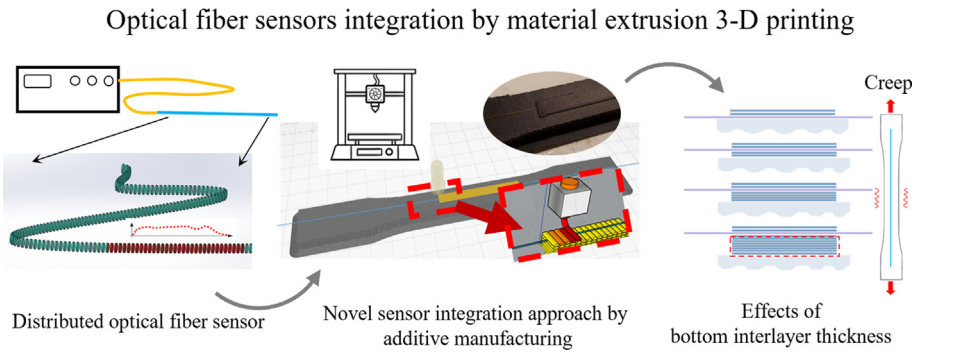

ARTICLE INFO

Article history:
Received 17 February 2022
Revised 29 June 2022
Accepted 30 June 2022
Available online 2 July 2022

Keywords:
Thermoplastic composite
Optical fibre
3-D printing
Structural health monitoring
Semi-automation

ABSTRACT

Thermoplastic composites are becoming the materials of choice for lightweight structures. Distributed optical fibre sensors can be valuable for structural health monitoring of thermoplastic composites, improving safety against damage and extending the operational life of composite components. However, the practical integration of optical fibres into thermoplastic composites remains still to be solved. To this end, a novel sensor integration approach by 3-D printing is proposed, and mechanical testing is conducted to test its performance. Optical fibres were placed inside thermoplastic embedding elements at controlled interlayer thicknesses (0 to 1.6 mm) from the substrate surface. Self-sensing experiments by optical fibres identified a uniform level of residual strains at −1600 με from the 3-D printing attachment process. Furthermore, tensile creep testing (up to ca. 1% strain) revealed that distributed strain transfer coefficients for optical fibre sensors remain constant with time. A simple calculation method that accounts for the shear lag effect between the component and optical fibre strains was derived from previous analytical work. This method enables the empirical prediction of strain transfer coefficients for optical fibre surface attachments with arbitrary embedding interlayer thickness.

1. Introduction

Fibre reinforced thermoplastic composites are becoming more popular over the entire spectrum of industrial and commercial applications. Their success over thermoset composites is attributed

* Corresponding author.
E-mail address: shaoquan.wang@ntnu.no (S. Wang).

https://doi.org/10.1016/j.matdes.2022.110914
0264-1275/

to better recyclability, lower manufacturing cost, and a good impact resistance [1]. Meanwhile, accurate and robust structural health monitoring (SHM) techniques are needed to ensure a safe operational life of thermoplastic composite components. Onboard sensor systems enable online monitoring, early detection of damage, and allow to extend the lifetimes of components based on their actual mechanical performances [2]. Compared to single-point or quasi-distributed fibre optic sensors such as Fibre Bragg Gratings (FBGs), distributed optical fibre sensors (DOFS) are preferred for high spatial resolution SHM of composite structures [3–6].

Any optical fibre (OF) strain sensor needs to be integrated into the composite material so that it deforms together with the component [7]. Thus, the OF performance depends to a large degree on the integration/attachment technique [8–10]. For example, optical fibres can be placed directly inside the composite material, between layers of thermoplastic tapes during the layup, which are then fused together with embedded OFs inside [11]. By using this method, strain from the component is directly transferred to the OF while the surrounding material protects the fibre sensor from the hostile environment [12–14]. However, there are also disadvantages to using this embedding method for OF integration. Voids or resin pockets are sometimes created around the embedded optical fibre which can locally affect the strength of the composite [15]. Embedded optical fibre becomes invisible to the eye and its accurate positioning within the structure is difficult to assess. Furthermore, optical fibres can encounter a high loss in transmitted/reflected signal power from bending at the edges of the laminate, or within the fabric structure which can induce micro-bending. High shrinkage of matrix material brings a birefringence effect to the OFs, leading to distortions of the measured signal spectrum instead of peak shifting [13]. Finally, the OF placement cannot usually be chosen with great flexibility during embedding, e.g. the intended ingress and egress regions may not be compatible with the manufacturing process.

Alternatively to embedding, OFs can also be bonded on the surface of a composite component after completing the manufacturing process [16–18]. Surface-bonding allows for more flexibility in attaching the OFs. It gives better opportunities for retrofitting existing structures with sensors, and for replacing damaged OFs with new ones. A thin bonding element on the surface can be removed or added without affecting the internal structure of the component if broken OFs are to be replaced. Admittedly, the surface-bonding solution has also some disadvantages that impair its suitability for lifetime monitoring of thermoplastic composites. Most structural adhesives are thermosetting polymers, and thermoplastics have poor adhesion with them due to their inherently low reactivity, surface energy and insufficient diffusion between the two materials [19–21]. Thermoset adhesives such as cyanoacrylate are also sensitive to the environment, they can have poor temperature or humidity resistance. Some adhesives need to be cured at a high temperature which is inconvenient and introduces heat into the host structure. Excessive amount of adhesive can induce a non-uniform bonding thickness and thereby a non-uniform strain transfer from the substrate to the surface-bonded sensor [22].

The attachment of optical fibres continues to be a manual process, thereby requiring careful working procedures and highly skilled assemblers. Automated solutions for bonding optical fibre sensors to thermoplastic composite materials have not yet become widespread [14,23]. For example, a semi-automated OF integration method during the braiding process of thermoset composites has been reported [23]. The optical fibre is placed between dry carbon fibre layers, and the bonding of the optical fibre to the composite is achieved later in the resin infusion process. However, this method cannot be directly used for thermoplastic composites. Automated methods are often developed for particular applications, resulting in lower flexibility in terms of product variety [24]. At the same time automated solutions help to improve product quality and consistency, adding the possibility of producing larger components, reducing material waste, and enabling easier in-process monitoring.

Out of all other alternatives, thermoplastic fusion bonding is perhaps the most practical solution for attaching optical fibre sensors to thermoplastic composites [25]. Additive manufacturing is popular for fabricating small-volume structures with complex structural geometries. Recently, the integration of OFs by 3-D printing has attracted the attention of several researchers. For example, point sensing FBGs have been embedded into metals during fused additive manufacturing (FDM) [26–28]. FBGs have also been embedded into 3-D printed polymer components again by using FDM, as reported by Karalekas et al. [29–31], Leal-Junior et al. [32,33], Manzo et al. [34], Nascimento et al. [28] and Falcetelli et al. [35]. Distributed OF sensors were embedded in titanium parts by Zhou et al. [36] using laser powder bed fusion. Inspired by this work, Wang et al. developed the embedding strategy for distributed OF sensors by in-situ FDM [37]. The most recent investigation by Wang et al. [38] compared different optical fibre surface attachment methods including the in-situ FDM process. Sensor integration attempts by 3-D printing are still in an early stage of research and only a few reference works are available. For embedded optical fibres, the difficulty of strain measurements with low infilling densities has been a typical research topic [32] along with some interest about residual strain measurements [37].

Ideally, strains from the surface bonded OFs should be equal to strains of the host structure. However, strain transfer errors through the attachment layer cannot be fully avoided. Previous researchers have numerically investigated important factors that affect the strain transfer coefficients from the substrate to the adhered FBGs [9,39,40]. The results show that thickness of the interlayer (i.e bondline thickness between the structure and the OF sensor) is a very important parameter, along with the length of the FBG sensor and the Young's modulus of the attachment layer [39–48]. Correlation between the geometrical parameters of the attachment layer and the strain transfer to the surface-bonded FBGs has been investigated by using analytical models and the FEM [40–45]. On this topic, experimental investigations and the validation of numerical models are much more rare. The influence of bottom interlayer thickness has only been analyzed by numerical simulations thus far, unlike the effects from the Young's modulus and the bonding length, which have also been experimentally investigated [39,40,43,46–48]. The most likely reason is that a consistent OF attachment thickness with prescribed values is difficult to produce by conventional hand-controlled surface bonding methods.

This research proposes a novel solution for semi-automated integration of distributed OF sensors on the surface of thermoplastic composite structures. Single mode optical fibres are in-situ embedded by material extrusion 3-D printing into block-shaped embedding elements on the surfaces of dogbone specimens. Short-fibre reinforced thermoplastic composite is extruded over the OF sensor at a controlled interlayer thickness. Distributed strain sensing system is achieved by using Rayleigh backscattering. Strain measurements by optical fibres are compared to contact extensometer strains in a tensile creep test. An experimental investigation on how the bottom interlayer thickness affects the strain transfer behavior of the DOFS has been carried out.

2. Materials and methods

Before mechanical testing, short carbon fibre reinforced polyamide (CF/PA6) specimens were prepared for the sensor integration

process. These specimens were produced by 3-D printing and the additive manufacturing process was thereafter continued for the OF integration on their surfaces. Optical fibres were placed inside small blocks of extruded thermoplastic called embedding elements, at a controlled thickness from the substrate surface.

2.1. Specimen preparation

Fused Filament Fabrication (FFF) i.e. small scale material extrusion is the most widely used manufacturing process within thermoplastic additive manufacturing. This method is also used by the PRUSA I3 MK3S 3-D printer, which was first employed to build the test specimens, and later for sensor integration purposes. Nylon 6 based composite filament (CF/PA6) from PolyMide (20 wt% chopped carbon fibres) and the dogbone specimen geometry were selected to build the test structure. Dogbone shape is very convenient for realizing a uniform tensile creep loading. A line pattern with 100% infill density and a quasi-isotropic layup sequence $[90,45,0,-45,]_{4s}$, where 0° angle denotes the longitudinal direction of the specimen, were employed to print the test specimens. Remaining printing parameters are detailed in Table 1.

Nylon 6 is known for good mechanical properties and its resistance to non-polar solvents [49]. Still, pure thermoplastic materials are rarely used for load-bearing components, due to their limited stiffness and strength. Composite components typically contain long fibre reinforcements along the main loading directions, which add stiffness, strength, and significantly reduce creep. Today, continuous fibre 3-D printing remains still technically challenging, and short-fibre reinforcements are much more popular with basic FFF printers, producing short-fibre reinforced polymer composites [50]. Creep strains in short-fibre reinforced composites are much higher than in any realistic long fibre reinforced composite laminates. In addition, the simple dogbone geometry allows to easily choose appropriate load levels for accelerated creep strain development compared to typical real-life composite structures. Therefore, compared to practical long-fibre reinforced composite structures, the specimen and the test set-up in this research provide larger/accelerated creep strain values for studying strain transfer from the component to the optical fibre sensor. In principle, similar 3-D printed OF attachments as used here can be realized with any type of thermoplastic composite provided that the matrix material and the resin of the embedding element are able to fuse and form a durable bond. In this sense, the choice of CF/PA6 composite material for this investigation is generic and arbitrary.

2.2. Sensor integration

As shown in Fig. 1, instrumenting the dogbone specimen occurs by means of embedding the optical fibre sensor into a specifically designed block-shaped embedding element. This embedding element is fabricated by the same printer and the same filament material on the surface of the specimen. The integration process is semi-automated and printing parameters are well-controlled. As previous work has showed, 3-D printing based integration process gives a more consistent bondline and promotes good measurement accuracy compared to other practical alternatives [38].

During operation, the 3-D printer is controlled by a modified G-code, which pauses printing after finishing a specific build layer where the optical fibre is integrated, and then resumes printing after a short delay. The OF attachment process (Fig. 1) follows a carefully planned procedure which can be summarized as follows.

(1) Preparation of two alignment holders with the same height as the finished layer.
(2) Placing the holders near the two ends of the specimen and placing the fibre on the last layer surface.
(3) Straightening the OF and fixing it on the alignment holders. Slight tension keeps the OF straight and controls its location on the specimen.
(4) Finishing the printing process and waiting for the system to cool down.
(5) Removing the alignment holders and detaching the instrumented specimen from the printing platform.

In order to investigate how the bottom thickness of the attachment layer affects measured strains, four different embedding configurations and a reference attachment with cyanoacrylate glue were realized. Dogbone test specimen is detailed in Fig. 2 and the specifics of embedding elements are further described in Table 2. For DOFS-0 configuration, the optical fibre sensor was placed directly on the surface of the dogbone specimen while the embedding element was printed from two layers of extruded composite. The first layer at 90° and the subsequent layer at 0°, each ca. 0.2 mm thick, were built directly on top of the optical fibre sensor. When the nozzle moves in zigzag motion at 90° relative to the OF, it 'sews' the sensor fibre to the substrate. The fibre becomes fully encapsulated after the 0° layer on top is finished. For DOFS-2 configuration, the fibre was embedded in the middle of the embedding element with two layers below and two layers above the fibre. For DOFS-4, the sensor had four layers below and two layers above it. For DOFS-8, the number of layers under the fibre grew to eight, while still only two layers were printed above the sensor. It must be emphasized that embedding elements DOFS-0 to DOFS-8 were kept identical in other aspects besides the bottom thickness T which varies between different attachment configurations. The influence of bottom interlayer thickness on the strain transfer from the host structure to the DOFS is experimentally investigated. Cyanoacrylate glue attachment DOFS-C was also introduced to this investigation representing the best performing 'traditional' surface attachment for distributed optical fibre sensors [38]. Due to the embedding element, the dogbone specimens were not symmetrical in the thickness direction as shown in Fig. 2. This non-symmetry can introduce additional strain for the tensile experiment, however its effect was assumed small and it was not studied further in this investigation.

2.3. Distributed strain sensing system

Distributed strain sensing system (Fig. 3) consists of an OBR 4600 device, a switch, a DOFS, and a laptop computer for running the hardware and storing the data. The optical fibre interrogator OBR 4600 (Luna Instruments) measures spectral shifts as a function of position along the optical fibre length. It utilizes Rayleigh backscattering to obtain distributed strain measurements. As the

Table 1
3-D printing parameters for CF/PA6 specimens.

Element	Material	Nozzle temperature	Build plate temperature	Printing speed	Cooling	Build- adhesion	Layer height
Dogbone	CF/PA6	290 ℃	45 ℃	50 mm/s	OFF	Brim	0.2 mm
Embedding element	CF/PA6	300 ℃	45 ℃	25 mm/s	OFF	None	0.2 mm

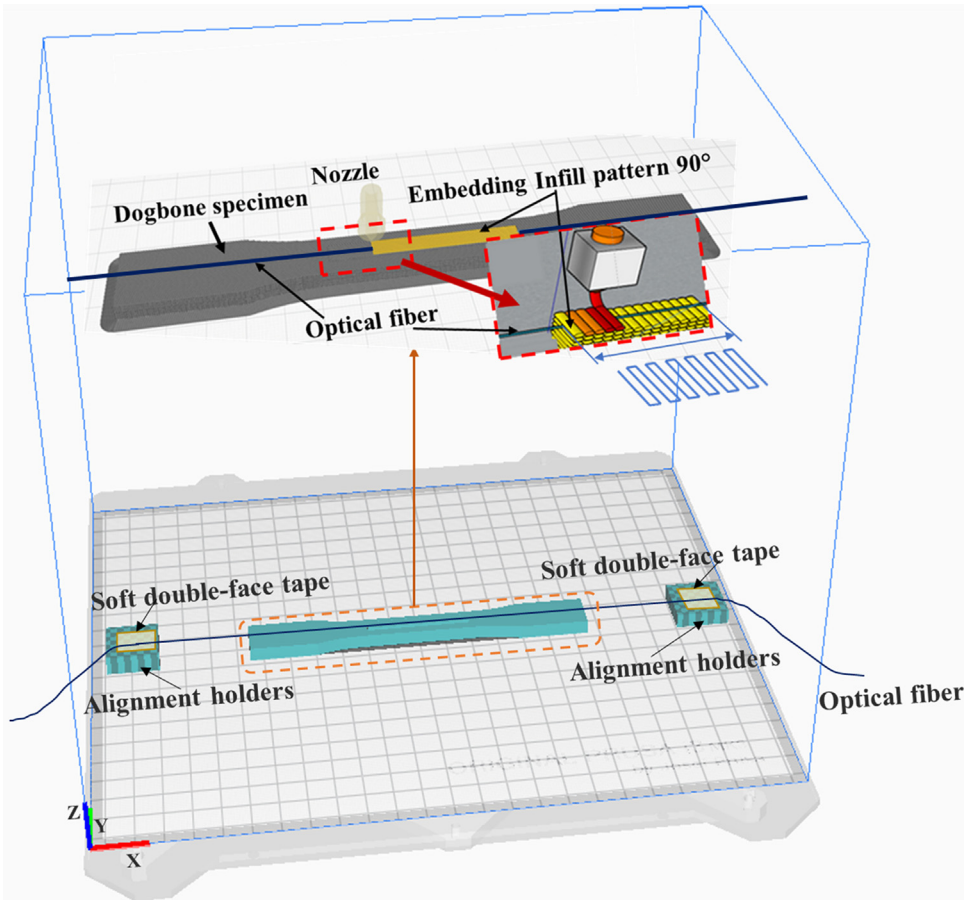

Fig. 1. Illustration of the optical fibre integration procedure.

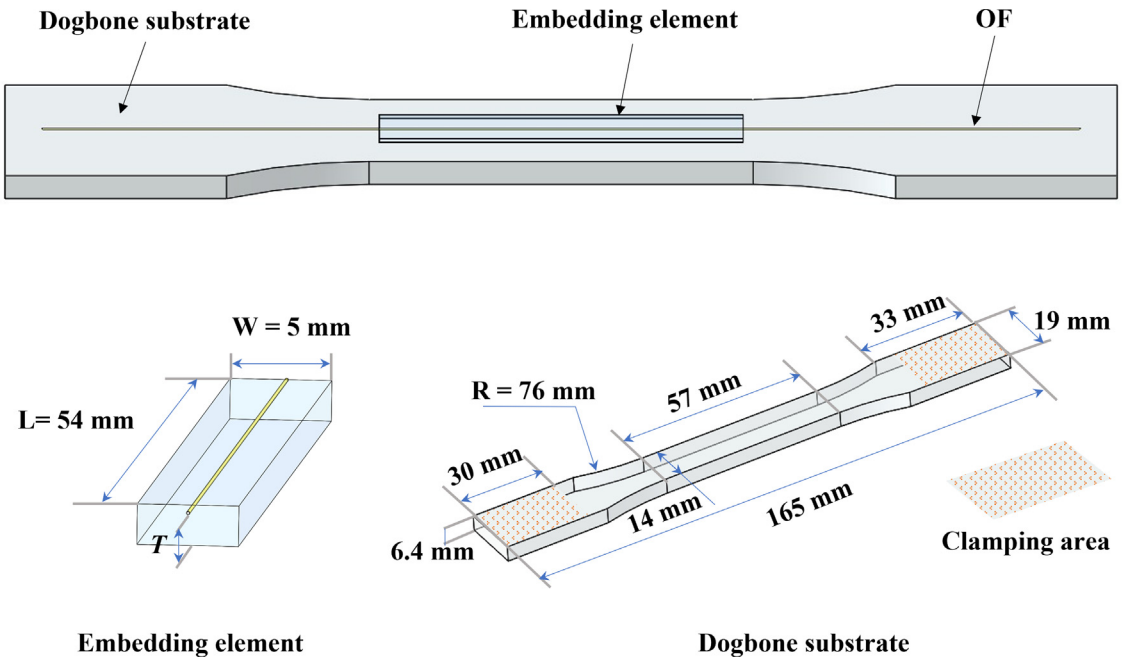

Fig. 2. Prescribed geometrical features of the dogbone specimen and the embedding element. The embedding element is placed symmetrically in the length and width directions, on one side of the dogbone.

optical fibre is mechanically strained, small changes in local Rayleigh backscattering spectra are calculated from the intrinsic variations reflected by the sensor fibre. These spectral shifts change proportionally to the amplitude of strain. In general, Rayleigh spectral shifts are affected by both strain and temperature. However, all measurements in this investigation are taken

Table 2
Optical fibre attachment configurations.

Attachment configuration	Bottom thickness *T*		Location of the optical fibre	Layup sequence of the embedding element
	No. of layers	Approximate thickness		
DOFS-0	0	less than 0.1 mm		[**OF** | 90,0]
DOFS-2	2	0.4 mm		[90,0 | **OF** | 90,0]
DOFS-4	4	0.8 mm		[90,0,90,0 | **OF** | 90,0]
DOFS-8	8	1.6 mm		[90,0,90,0,90,0,90,0 | **OF** | 90,0]
DOFS-C	N/A	N/A		'Cyanoacrylate'

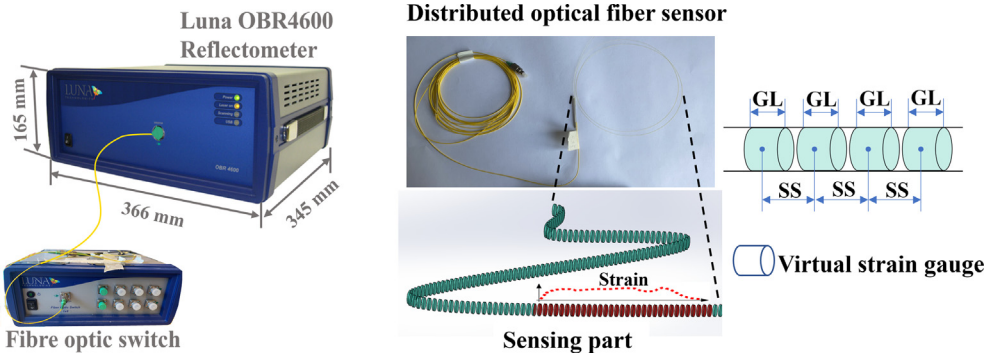

Fig. 3. OBR 4600 interrogator system and the distributed optical fibre sensor (DOFS).

at constant room temperature, so the temperature effects are assumed negligible for all practical purposes.

A single mode fibre SMB-E1550H from OFS Fitel is employed as the distributed optical fibre sensor. The diameters of the core, the cladding, and the coating of this silica/silica/polyimide fibre are 6.5 μm, 125 μm and 155 μm, respectively. The laser in the OBR 4600 device sends light pulses through the optical fibre, and reflected Rayleigh backscattering spectra are measured by the same interrogator and stored in the computer memory. By comparing the spectra before and after mechanical loading, strains along the optical fibre are calculated. The measurement system offers practical spatial resolutions below 1 cm, a strain resolution of 1 με, and a sensing length of ca. 50–70 m [51]. The post-processing configuration with sensor spacing SS = 0.5 mm, and gauge length of GL = 5 mm was chosen as a compromise between high spatial resolution and unwanted noise occurrences. By choosing this 5 mm gauge length value, each virtual strain sensor along the optical fibre has been assigned the typical dimension of a physical strain gauge. Much shorter sensor spacing indicates that virtual strain sensors on the DOFS are overlapping. These two parameters were selected based on quick trials with the test data, and on previous experiences from similar measurements.

2.4. Creep testing

Mechanical testing of dogbone specimens was performed on a MTS Model 42 universal testing machine. The test set-up is shown in Fig. 4(a). Test machine fixtures clamp the ends of the dogbone specimens at a length of 30 mm as seen in Fig. 2. The creep load-time curve is presented in Fig. 4(b). All specimens were initially loaded up to a small pre-load of 15 N, and then further until 1800 N using a cross-head speed of 100 mm/min. This loading produced initial (short-term) strains of approximately 8000 με. A short adjustment period of less than 40 s was necessary due to the control-loop programming before the load settled to a constant value at time t_2. Creep loading was maintained constant with less than 1 N variation and the test was stopped at 1 h after t_2.

Strains were recorded every 120 s from time t_2 until the end of the experiment. Strain of the dogbone was simultaneously monitored by the DOFS system and the contact extensometer (EXT) set-up, as shown in Fig. 4(a). Extensometer Instron 2620–601 has a gauge length of 50 mm. Its knife edges were mounted on the side of the composite specimen to measure averaged strain along the same region where the DOFS was attached.

Two different baseline references were used to calculate both the DOFS and the contact extensometer (EXT) strains. References taken before the DOFS were fixed on the specimens (i.e. when the fibres were free) are hereby denoted as free-fibre references. Accordingly, strains calculated by comparing to the free-fibre reference are called *relative free-fibre strains*. Another reference was taken at time t_2 of the creep test. Similarly, strains obtained by comparing to the reference at t_2 are called *relative-t_2 strains*. As evident from the load-time curve in Fig. 4(b), relative-t_2 strain represents only the time-dependent portion of strain development during tensile creep, excluding short-term strain from the load ramp-up procedure.

Although only one specimen for each configuration (Table 2) is reported in this paper, two additional specimens were internally fabricated and tested for each configuration. These two additional tests yielded very repeatable results. Therefore, for the sake of clarity in the figures and to reduce the volume of the paper, only one specimen for each test configuration is hereby reported.

3. Results and discussion

As previous investigation has demonstrated [38], the bondline consistency of optical fibre surface attachments varies a lot

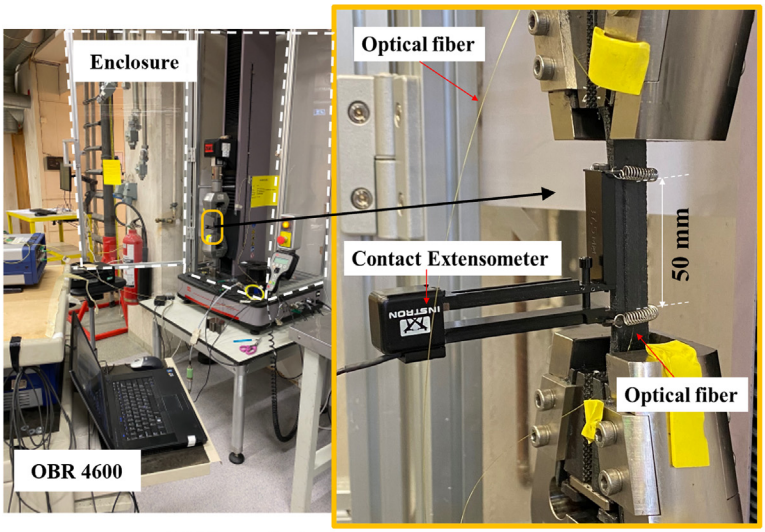

(a) Two strain measurement systems

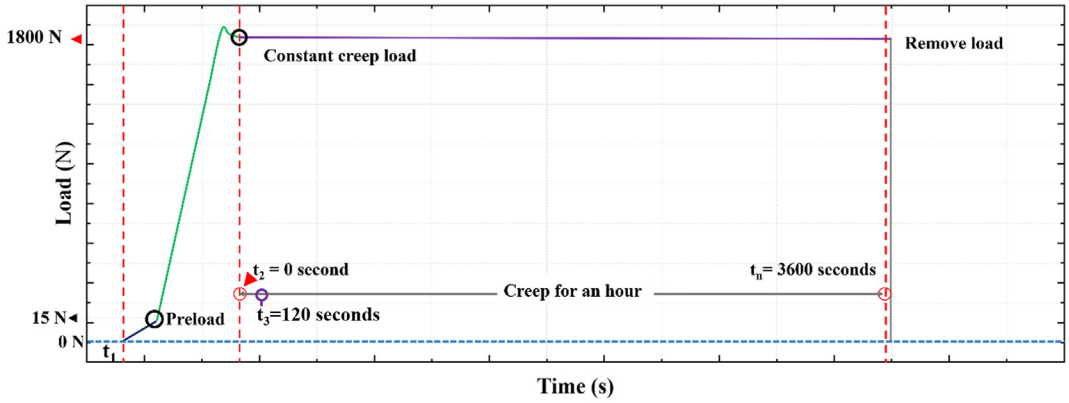

(b) Load-time curve

Fig. 4. Experimental test set-up.

between different attachment methods. Imperfections such as small cracks and the misalignment of the OF can cause noisy data-points and local distortions in the DOFS strain profile. Bottom interlayer thickness between the optical fibre and the substrate surface also holds a high degree of uncertainty. This interlayer thickness is difficult to control in hand-operated optical fibre integration processes. Furthermore, since high-resolution computed tomography equipment is not widespread, measuring the bottom thickness is typically a destructive process that involves cutting, polishing, and optical microscopy. On the other hand, the bottom thickness value can be easily prescribed for a machine-controlled attachment process, e.g. when using the 3-D printing principle. The effect of bottom interlayer thickness on distributed optical fibre strains has not been experimentally investigated until now.

In the following, residual strains and creep strains from varied bottom interlayer thickness optical fibre placements are experimentally compared. Strain curves obtained from 3-D printed OF sensor attachments are also compared to a typical high-accuracy attachment method using cyanoacrylate glue. In addition, OF strains are compared to contact extensometer strains within the same dogbone specimen gauge length.

3.1. Embedded length (EL), region of interest (ROI) and peak value

Along both, load free fibres and strain-loaded optical fibres, a fluctuation of strains within ca. ± 5 με is considered a normal level of noise. It is present everywhere on the DOFS and these small strain variations are usually ignored in the measurement [52]. By measuring the length of the region where strains exceed this normal level of noise, the true embedded length of the fibre (denoted as EL in Fig. 5) can be obtained. The Table in Fig. 5 shows true DOFS embedded lengths (Els) obtained by measuring where the strain exceeds ± 5 με of signal noise, from Fig. 6 (a)-(d). The Els for DOFS-0 to DOFS-8 were all prescribed for 3-D printing as 55 mm. The Els obtained from residual strain values vary within 53.0 ± 5 m m and 58.5 ± 5 mm. Considering the size of the extrusion bead, the tolerances of the specific printer, and the virtual DOFS gauge length of 5 mm (which is assumed to govern the error [38]), this is a good agreement between the design aim and the actual realized embedded length of the optical fibre sensor.

As Fig. 6 and further strain graphs show, in practical OBR measurements, the strains in the DOFS ingress and egress transition regions are observed to be highly variable. Thus, in order to meaningfully compare mean strains from the OBR measurements to averaged values of extensometer strains, these highly variable disturbed strains at the transition regions must be excluded from the analysis [38,53]. This way, only strains from the central region of the DOFS attachment, with relatively even strain distribution, are averaged to assess the strain state of the host component. This quasi-constant central region symmetric with respect to the length of the specimen, is referred to as region of interest (ROI). As shown in Fig. 5, disturbed regions located at the ingress/egress of the opti-

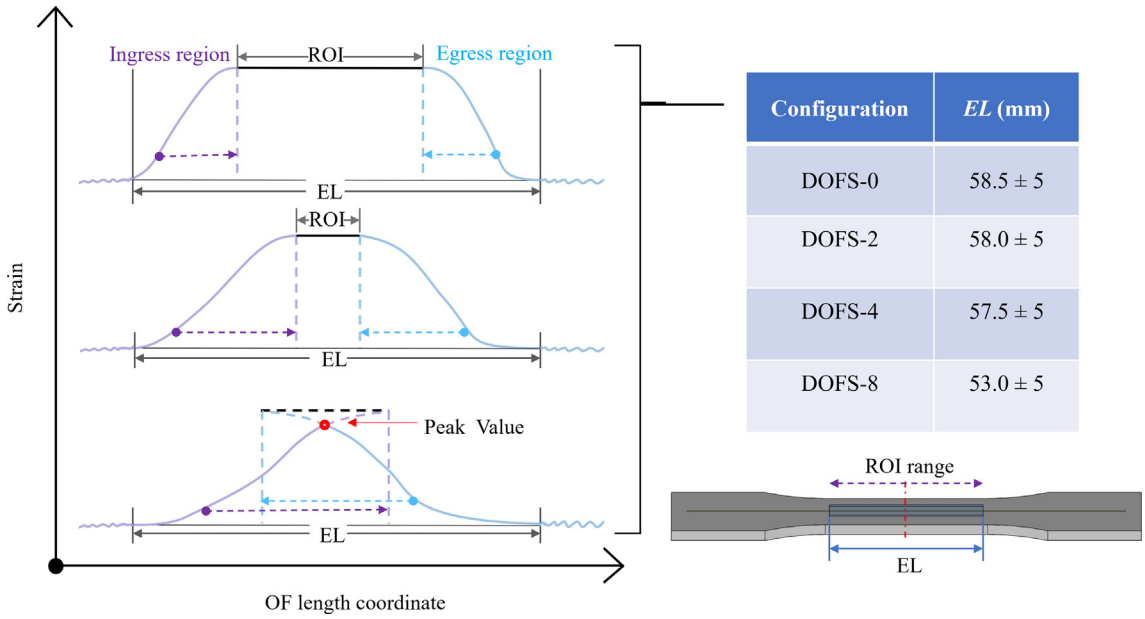

Configuration	*EL* (mm)
DOFS-0	58.5 ± 5
DOFS-2	58.0 ± 5
DOFS-4	57.5 ± 5
DOFS-8	53.0 ± 5

Fig. 5. Illustration of EL, ROI and Peak Value on simplified DOFS strain curves. The EL values in the Table are obtained from residual strain curves after 3-D printing (Fig. 6).

cal fibre attachment, define a transition between a free and an attached optical fibre. In the usual analysis, strains from the ROI are averaged when interpreting spatial strain curves from the DOFS. However, as illustrated in Fig. 5 and exemplified with measured strain curves later, with increasing the length of disturbed regions, which occurs with increasing bottom interlayer thickness, the central region forming the ROI becomes shorter or even disappears. In this case, the Peak Value can be used as an alternative characteristic or metric for DOFS strains.

3.2. Residual strains from the attachment process

During the optical fibre attachment process, residual strains can be built into the host structure of the optical fibre sensor. Residual strains are created from changes in the material constitution (such as cure shrinkage of thermosets and changes in crystallinity of thermoplastics), and from physical volumetric shrinkage when the hot material cools down to room temperature. Residual strains and corresponding residual stresses remain 'frozen in' inside the component without any external mechanical loading. When measuring residual strains with optical fibres, the pre-attachment free fibre is taken as the reference state, and the load free room temperature condition after the fibre integration as the measurement state. That is, relative free-fibre strain is measured after the attachment process is finished.

As defined in Table 2, the DOFS were attached according to four embedding configurations and were also bonded by a cyanoacrylate glue as the control specimen. Residual strain distributions from the DOFS integrated with these five configurations are shown in Fig. 6. The profiles from 3-D printed attachments in Fig. 6(a)-(d) display very similar bathtub shapes with occasional outliers in the ingress/egress regions. In contrast, residual strains from the cold-curing cyanoacrylate attachment DOFS-C (Fig. 6(e)) are much smaller and drift up and down chaotically along the embedded DOFS length. Fig. 6(f) compares the mean values, standard deviations (SD) and the coefficient of variation (CV) for attachments DOFS-0 to DOFS-8. Mean values and SDs are calculated from spatial residual strains within the ROI = 40 mm as shown in Fig. 6(a)-(d). CV is the ratio of SD to the absolute value of the mean. The mean values of residual strains for DOFS-0 to DOFS-8 vary within 1500 με and 1750 με in compression and the CVs range from ca. 2.0% to 5.5%. No monotonic trend with increasing embedding bottom thickness was observed for different attachment configurations. The mean values of residual strains turn out to be independent of the small variation in embedding bottom thickness.

In summary, all 3-D printed attachment configurations produced nearly uniform compressive residual strains of ca. 1600 με along the OF sensor length. These strains are created by the cooling shrinkage of the polymer melt together with a few layers of re-heated substrate material. In comparison, the tiny residual strains from the cyanoacrylate glue (between ± 70 με) were created in a fully room-temperature process, by a combination of locally variable compressive shrinkage of the glue and a small tensile pre-stretch applied by hand, when aligning the fibre during the attachment process [38]. This resulted with a random variation of small strains along the optical fibre length.

3.3. Creep strain analysis

Many structural components are monitored under long-term loading conditions. To understand time-dependent strain transfer from the host structure to the surface bonded optical fibre better, uniaxial tensile creep testing was carried out with dogbone specimens. Throughout creep loading, strains within the specimen gauge region were measured with the attached DOFS and the contact extensometer (EXT) simultaneously. This investigation focuses on time-dependent strain development, thereby discarding the initial short-term strains. Relative-t_2 strains of the DOFS and the extensometer were recorded. The influences of time and embedding bottom thickness T on distributed strain development were experimentally investigated.

3.3.1. Relative-t_2 creep strains

Fig. 7(a), (d), (g), (j) show relative-*t2* spatial strains from the DOFS attached by 3-D printing with different embedding bottom thicknesses. For comparison, Fig. 7(m) shows relative-t_2 strains when using the traditional cyanoacrylate glue attachment. Note that the vertical axis range is the same for all strain curves on Fig. 7. Relative-t_2 strains from different bottom thickness configurations show distinctly different spatial distribution patterns. For

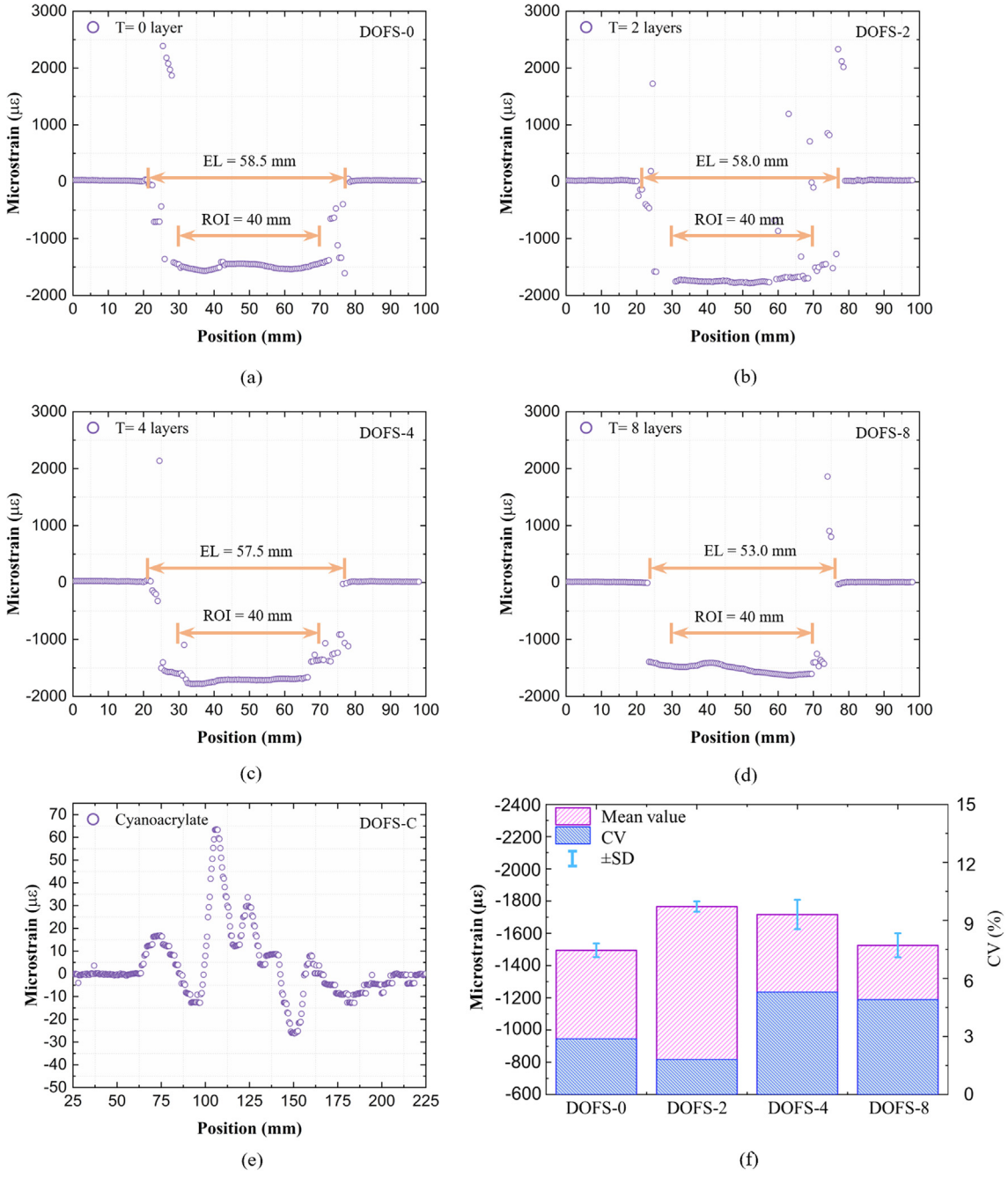

Fig. 6. DOFS measured residual strains for different attachment configurations.

example, DOFS-0 and DOFS-C show a spatial strain distribution again similar to a 'bathtub'. Strain values increase gradually in the ingress region, decrease gradually in the egress region, and hold a nearly constant plateau value in the middle. By increasing the embedding bottom thickness, the length of the plateau however shortens (DOFS-2) and finally disappears (DOFS-4 and DOFS-8). The shape of the spatial strain curve begins to display a peak where the plateau used to be. With the creep time increasing, relative-t_2 strains of the DOFS also keep on increasing. At first sight, no significant distortions emerge on the strain profiles, indicating no cracking or delamination in the specimen or at the optical fibre/matrix interface during creep.

Fig. 7(b), (e), (h), (k), (n) show temporal average relative-t_2 strains and peak value strains from all attachments, using the data over the gauge length of the contact extensometer, i.e. ROI = 50 mm. As seen from the spatial strain plots, this ROI includes transition regions at the ingress/egress of the optical fibre for all types of attachments. Strain measurements from the attached DOFS are compared to the EXT strains from the contact extensometer. The difference between DOFS strains and EXT strains is further elaborated in Fig. 8(c), (f), (i), (l), (o) by calculating absolute differences $C_A(t)$ and relative differences $C_R(t)$, as defined by Eqs. (1) and (2).

$$C_A(t) = |\varepsilon_{DOFS}(t) - \varepsilon_{EXT}(t)| \tag{1}$$

$$C_R(t) = \left|\frac{\varepsilon_{DOFS}(t) - \varepsilon_{EXT}(t)}{\varepsilon_{EXT}(t)}\right| \times 100\% \tag{2}$$

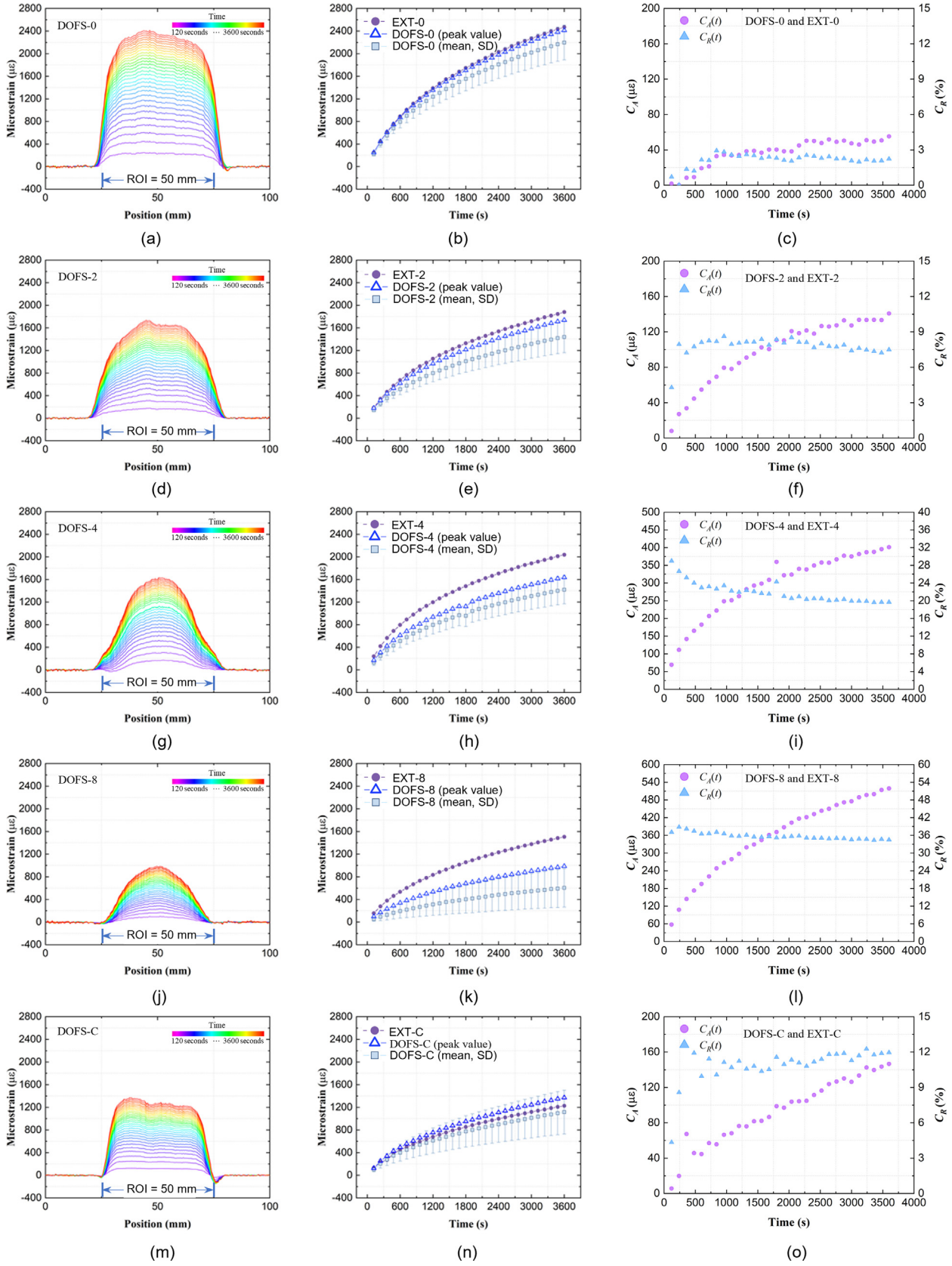

Fig. 7. Relative-t_2 creep strains from the DOFS and the contact extensometer (EXT).

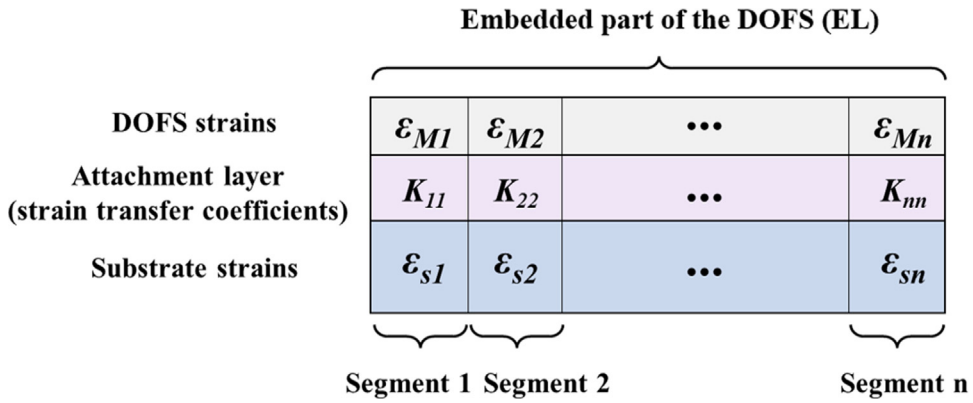

Fig. 8. Discretization of the substrate/attachment/DOFS structure.

In these Equations, $\varepsilon_{EXT}(t)$ denotes relative-t_2 strains from the extensometer, while $\varepsilon_{DOFS}(t)$ are defined as the peak values of the DOFS strain curves within the ROI.

The thinnest 3-D printed attachment DOFS-0 and the cyanoacrylate glue display the best agreement between extensometer strains and peak relative-t_2 strains from the optical fibres. The peak values and the extensometer strains are also very close for the slightly thicker DOFS-2 attachment. For all attachments, the absolute difference $C_A(t)$ continues to increase with increasing of the creep time, while the relative difference $C_R(t)$ flattens out after initial transient and then remains almost constant.

From specimens DOFS-0 to DOFS-8, the differences between average relative-t_2 strains and EXT strains quickly increase with the increase of the bottom interlayer thickness. Meanwhile, as the plateau region shortens to zero, average strains within any length of ROI, let alone ROI = 50 mm, are not suitable for interpreting the strain curves anymore. The plateau region simply ceases to exist. Alternatively, the peak values of DOFS strains can be used as a strain characteristic. However, the peak values are still smaller than EXT strains and the $C_A(t)$ shows an increasing trend of growth with both the increase of bottom interlayer thickness and with elapsed time. The relative difference $C_R(t)$ on the other hand remains nearly constant with time, increasing rapidly from 2.5% to 36% with only ca. 1.6 mm increase of bottom interlayer thickness. This monotonically increasing disagreement between DOFS strains and EXT strains indicates an increasing strain transfer lag in the embedding element caused by a larger bottom interlayer thickness.

Main highlights of the experimental data are summarized as follows. Strain measurement accuracy of DOFS-0 is comparable to using a high-accuracy cyanoacrylate attachment. However, a strain transfer lag develops quickly when increasing the bottom interlayer thickness. And finally, the relative difference $C_R(t)$ between extensometer and optical fibre strains remains approximately constant under creep loading conditions, for all tested configurations of DOFS attachments. This confirms similar findings first noted in [38].

3.3.2. The effect of time on strain transfer coefficients

Strain transfer coefficients of DOFS which are attached by low-creep thermoset adhesives, e.g., to CFRP laminates or to steel, are often viewed as constant in time. Meanwhile, the viscoelastic mechanical behavior of CF/PA6 thermoplastic composite causes much larger time-dependent deformations in creep; thus, it is essential to understand if and how does time play a role in the strain transfer process. The challenge lies in that both the substrate and the attachment layer are built from the same polymer composite material with highly time dependent mechanical properties.

As illustrated in Fig. 8, the substrate/attachment/DOFS structure can be discretized into n segments along the length of the DOFS-substrate adhesive joint. It is assumed that no slip occurs in the attachment. Using this framework, the strain distribution along the attached DOFS can be expressed by using a diagonal strain transfer matrix K_{ii}, as follows:

$$\begin{Bmatrix} \varepsilon_{M1} \\ \varepsilon_{M2} \\ \varepsilon_{M3} \\ \vdots \\ \varepsilon_{Mn} \end{Bmatrix} = \begin{bmatrix} K_{11} & 0 & \cdots & \cdots & 0 \\ 0 & K_{21} & 0 & \cdots & 0 \\ \vdots & 0 & K_{33} & 0 & \vdots \\ \vdots & \vdots & 0 & \ddots & 0 \\ 0 & 0 & \cdots & 0 & K_{nn} \end{bmatrix} \begin{Bmatrix} \varepsilon_{s1} \\ \varepsilon_{s2} \\ \varepsilon_{s3} \\ \vdots \\ \varepsilon_{sn} \end{Bmatrix} \tag{3}$$

where K_{ii} are the strain transfer coefficients between substrate strains ε_{si} and DOFS strains ε_{Mi} for the i_{th} attachment segment. The initial set of coefficients K_{ii} can be calculated by adopting DOFS strains and EXT strains at t_3 = 120 s, as illustrated in Fig. 4(b). Extensometer strains represent substrate strains ε_{si}, which are considered equal/constant at every segment i along the length of the OF attachment. The DOFS strains ε_{Mi} are obtained from the embedded length (EL) of spatial strain curves in Fig. 7 and each segment i corresponds to one virtual strain gauge on the optical fibre. Initial strain transfer coefficients K_{ii} are calculated by using $K_{ii} = \varepsilon_{Mi}/\varepsilon_{si}$ from Equation (3), and plugging in the measurement data ε_{Mi} (DOFS) and ε_{si} (EXT) from the first time point $t_3 = t_2 + 120$ s. The choice of initial time point t_3 is arbitrary and a very similar analysis to what follows is produced by selecting e.g t_2 + 240 s or t_2 + 360 s as the initial point in time.

As a first approximation, it is assumed that strain transfer coefficients K_{ii} remain constant in time. In this case, the DOFS strain profiles at a later time $t = t_n$ can also be predicted by Equation (3) by using the initial transfer matrix K_{ii} times extensometer strains ε_{si} at $t = t_n$. In this way, the DOFS strain profiles at t_n = 960 s, 1800 s and 3600 s are predicted and compared to actual measured DOFS strains in Fig. 9. For DOFS-0, DOFS-2 and DOFS-8, predicted strains match well with experimentally measured strains, all along the DOFS length, and all throughout the creep process. These results support the hypothesis that temporal variation does not affect the strain transfer coefficients K_{ii}.

It can be observed from Fig. 9(c), that predicted strain values of DOFS-4 were noticeably smaller than measured strains, and their distribution patterns had also changed at the ends of the embedded DOFS. For DOFS-4, the creep strains had developed faster than anticipated. One possible interpretation is that some imperfections (micro-cracks, local yielding) had developed at both ends of the DOFS early during the creep loading process. All other things equal, imperfections or damage are expected to appear at the ends of the bondline where stress concentrations are the highest. Looking

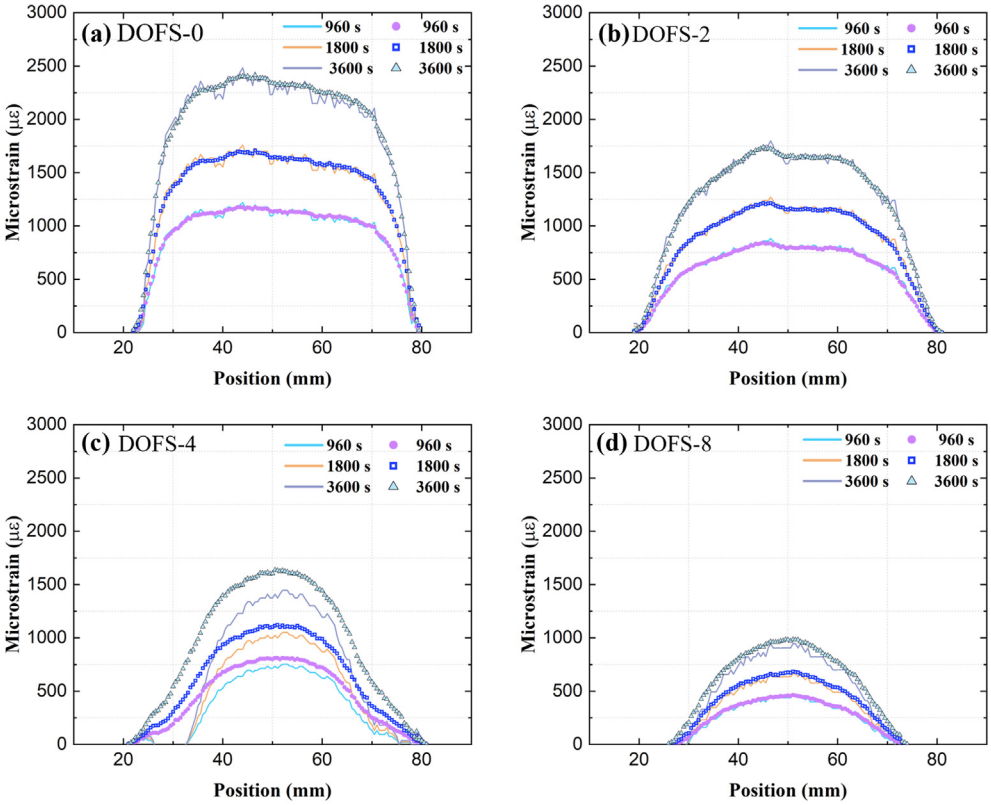

Fig. 9. Comparison between predicted (line) and measured (markers) relative-t_2 strains along the embedded DOFS at three distinct time points (Markers appear like a thick line).

back, the existence of possible imperfections at the ends of DOFS-4 was vaguely implied from early on, in the residual strain profile in Fig. 6(c).

3.3.3. The influence of bottom interlayer thickness

As the strain graphs in Fig. 7 showed, the thickness of bottom interlayer T affects the strain transfer behavior significantly. By increasing bottom interlayer thickness, the quasi-constant strain plateau in the middle of the attachment becomes contracted. Furthermore, the peak values of strain curves are also increasingly lower.

It is well known that specimens made by extrusion based 3-D printing still suffer from inconsistencies from the production process. This may cause a higher dispersion in material properties, compared to other more established manufacturing methods. To account for specimen-to-specimen variability, the DOFS strains of Fig. 7 are normalized by their corresponding EXT strain values in Fig. 10. This Figure shows normalized relative-t_2 DOFS strain profiles from specimens DOFS-0 to DOFS-8 at the beginning (t = 120 s) and at the end (t = 3600 s) of the creep test. Strains from the contact extensometer, constant at 100%, are also shown on the same Figure by horizontal red lines. The midpoints as well as the start/end points of the EXT gauge area are indicated by vertical dashed lines.

It is easy to recognize that normalized DOFS strain curves now display the strain transfer coefficients visually. Along the optical fibre, most of the DOFS strains are smaller than substrate strains (EXT strains) depending on the bottom thickness T of the embedding element. The left and the right columns of the Figure are nearly identical, confirming again that time does not significantly affect the strain transfer coefficients. However, by increasing the bottom thickness T, difference between DOFS strains and EXT strains increases monotonically. Both the normalized strain magnitude and the shape of the strain curve change simultaneously. As Fig. 10 shows, by increasing the bottom interlayer thickness, the height of strain curve decreases, and the width of the curve contracts. The plateau shortens from DOFS-0 to DOFS-2 and transfers into a peak in DOFS-4. By further increasing the bottom thickness T in DOFS-8, the curves become narrower, and the peak sharpens. It can be concluded that bottom interlayer thickness T affects the DOFS strains in two ways: i) by increasing T the length of the ingress/egress, i.e. the strain gradient regions increases, and ii) by increasing T the peak values of DOFS strain curves decrease. The most likely reason is the 'shear lag' effect from the attachment layer. Similarly, this 'shear lag' effect has been shown to induce monotonically increasing/decreasing strain gradients for the FBG strain sensors in a number of earlier studies [41–47].

3.4. Shear lag correction

Both Fig. 7 and Fig. 10 have clearly demonstrated how distributed optical fibre strains do not agree with the extensometer, i.e. structural component strains, already when the embedding bottom thickness reaches 0.4 mm (DOFS-2) or larger. Any strain analysis that employs the bathtub curve from the DOFS sensor needs to account for this shear lag error. That is, DOFS strain curves must be interpreted to compare them with the uniform strain of the substrate that is measured by the extensometer. Reducing the length of the ROI (Fig. 5) is a simple practical method for discarding the ingress/egress regions of distributed strains [38]. However, as the experimental strain curves in Fig. 10 show, reducing the ROI alone is not sufficient to calculate strains from the DOFS measurement which are equal to the sub-

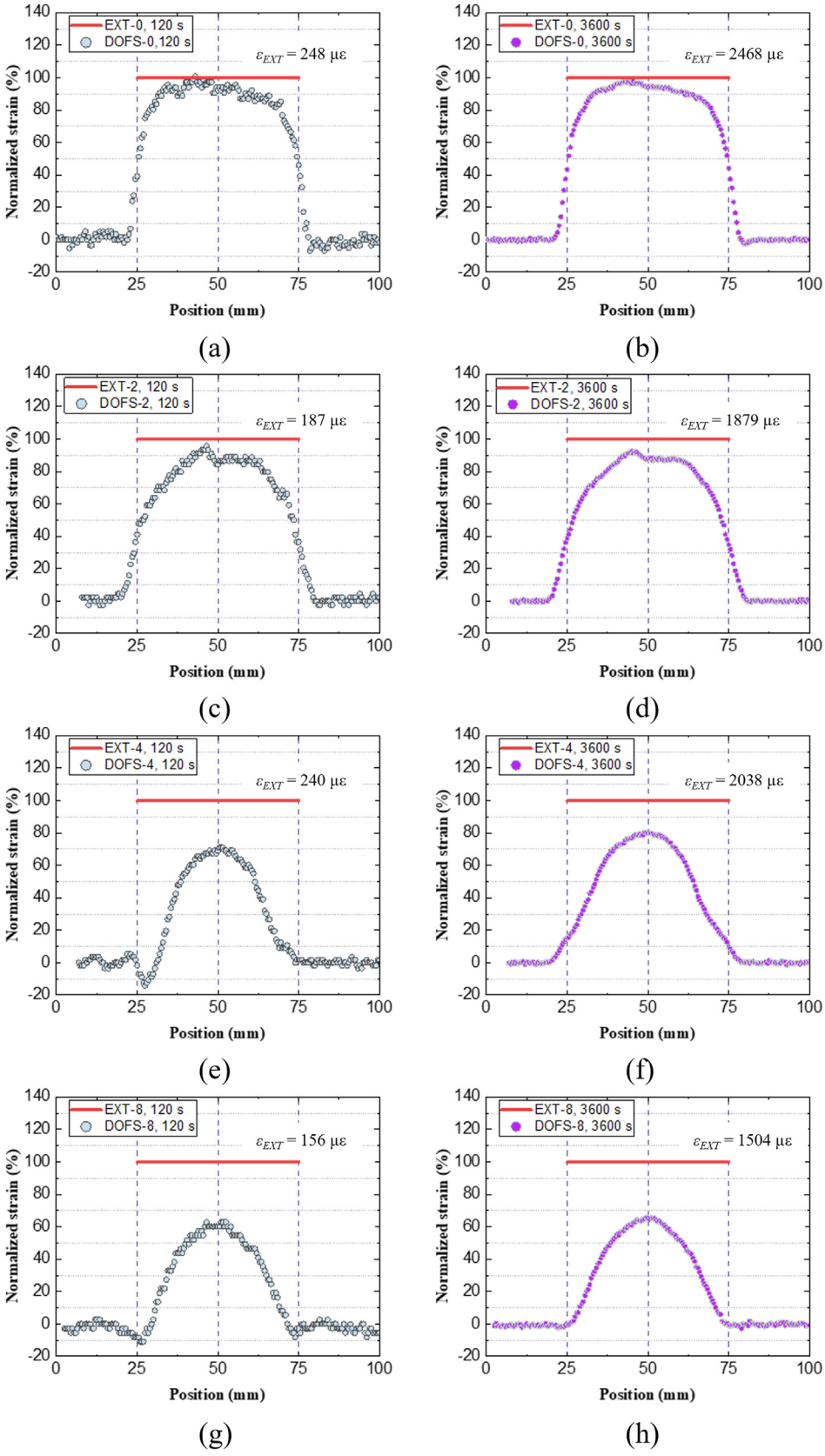

Fig. 10. Normalized relative-t_2 strains during tensile creep (at t = 120 s, t = 3600 s).

strate component strains (EXT strains). Experimental data shows that embedding bottom thickness T has a basic underlying influence on the DOFS strains. If accurate component strains are to be measured by optical fibres, the shear lag needs to be corrected, besides accounting for tapered strains at the ingress/egress transition regions.

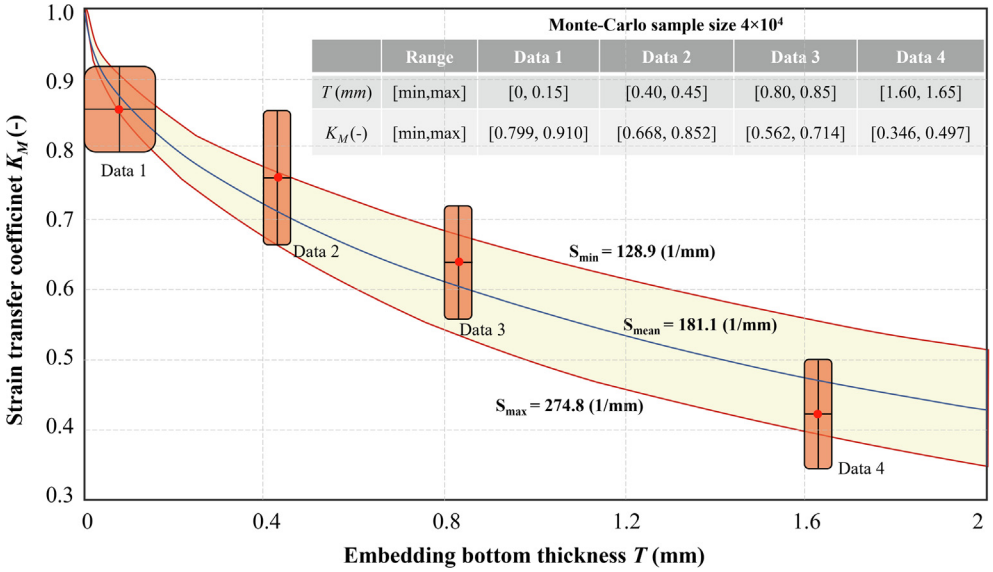

Fig. 11. Curve fitted strain transfer coefficients calculated from experimental data using the shear lag correction model.

As known from theoretical models of surface-bonded FBGs [41–47], the average strain transfer coefficient K_M for the FBG sensor can be expressed as:

$$K_M(T) = 1 - \frac{\sinh(\alpha)}{\alpha\cosh(\alpha)} \tag{4}$$

where T is the bottom thickness of the attachment layer (the same as in this investigation), and α is a 'hybrid' coefficient dominating the shear lag behavior between the substrate and the optical fibre sensor. This coefficient α combines material and geometrical properties of the optical fibre and the attachment layer. Although α can be expressed by complex equations using different variables in the analytical models [41], when bottom interlayer thickness T is considered as the only non-constant variable, it can be simplified as follows:

$$\alpha = \sqrt{\frac{1}{TS}} \tag{5}$$

Here, parameter S is a constant, independent from thickness T, and determined by the diameter and the modulus of the naked optical fibre, fibre coating, width of the bondline, etc. In this work, parameter S is considered as constant for all specimens with different embedding bottom thicknesses. Now, by substituting Eq. (5) into Eq. (4), the strain transfer coefficient is expressed as:

$$K_M(T) = 1 - \frac{\tanh(\sqrt{\frac{1}{TS}})}{\sqrt{\frac{1}{TS}}} \tag{6}$$

Consequently, when both thickness T and strain transfer coefficient K_M (T) are known from several test configurations (of one or more), a curve fitting procedure can be applied to obtain the missing constant S. Then, by inserting the obtained S value back into Eq. (6), any unknown strain transfer coefficient for DOFS with arbitrary bottom interlayer thickness T can be calculated.

Unfortunately, in this investigation the bottom interlayer thickness T can not be known precisely, even if the number of 3-D printed attachment layers under the DOFS are prescribed. During embedding, the optical fibre (Ø = 0.15 mm) is encapsulated within one 0.2 mm layer of melt, on top of previously 3-D printed and solidified layers of thermoplastic composite. To account for this vertical placement uncertainty, the value of bottom interlayer thickness is hereby estimated between the nominal bottom thickness T (Table 2) and T + (0.2 - Ø) mm, that is, in the range [T, T + 0.05] mm. The experimental strain transfer coefficients K_M (T) corresponding to aforementioned bottom interlayer thicknesses T have to be obtained similarly as ranges of values. As shown in Fig. 10, strain transfer coefficients of embedded DOFS vary along the optical fibre length. From these curves, a conservative estimate for the limits of the coefficient range is obtained by using ROI = 5 mm (captures the highest peak in the middle of the curve) and by averaging the entire curve by using ROI = 50 mm (which includes tapered/lower end regions). Based on these [min, max] ranges for the experimental values of T and K_M, a range of parameters S can be calculated by using Monte-Carlo sampling. The input data was generated uniformly over the range [min, max] for each test configuration, as shown in Fig. 11. An obvious characteristic relationship can now be observed for all calculated curves of K_M as a function of bottom interlayer thickness T. Strain transfer coefficients K_M are especially sensitive to the variation of T when T is small, e.g., less than 0.4 mm (DOFS-0, DOFS-2). This explains why varied strain data are often obtained from optical fibres when using hand-controlled attachment methods, even though only a thin bottom layer of glue exists between the optical fibre and the substrate. The method presented here enables to predict the value of strain transfer coefficient K_M for any unknown thickness T. By using the shear lag correction method, a more accurate substrate strain measurement can now be realized even when optical fibres are attached through a thick intermediate layer of material.

4. Conclusions

1. A novel 3-D printing based embedding method was presented for attaching optical fibre sensors on the surface of thermoplastic composite components.
2. Residual strains from 3-D printing based attachment process reached ca. −1600 με for short-fibre reinforced CF/PA6 composite used in this study. All residual strain curves remained constant along the attachment length and were independent of the bottom interlayer thickness.

3. Creep strain measurement accuracy that is comparable to cyanoacrylate glue was achieved by optical fibres embedded at zero interlayer thickness. However, by increasing the bottom interlayer thickness, a shear lag effect is quickly introduced between the substrate and the OF sensor strains.
4. Strain transfer coefficients along the attached optical fibres remain constant with elapsed creep loading time. Departure from constant values implies that some forms of imperfections (cracks, local yielding) are occurring at these locations of sensor attachments. However, any such stiffness degradation mechanism needs more experimental confirmation.
5. A simple semi-empirical calculation method was proposed for correcting optical fibre strains for the shear lag effect at an arbitrary interlayer thickness *T*.
6. For future experiments of the same type, a few recommendations are suggested for better experimental control. The embedding elements are suggested for both sides of the dogbone specimen (one dummy if necessary), and they should remain in the same volume for all test configurations. Also, live temperature measurements are recommended on the test specimen to confirm that no excessive heating occurs when applying the load.

Data availability

The data that has been used is confidential.

Declaration of Competing Interest

The authors declare that they have no known competing financial interests or personal relationships that could have appeared to influence the work reported in this paper.

Acknowledgment

This work was partially supported by the European Union's Horizon 2020 research and innovation programme and Hydrogen Europe and Hydrogen Europe Research (Grant ID: 826262).

References

[1] H. Ning, N. Lu, A.A. Hassen, K. Chawla, M. Selim, S. Pillay, A review of Long fibre thermoplastic (LFT) composites, Int. Mater. Rev. 65 (2020) 164–188, https://doi.org/10.1080/09506608.2019.1585004.
[2] M. Amafabia, D. Montalvão, O. David-West, G. Haritos, A Review of Structural Health Monitoring Techniques as Applied to Composite Structures, Struct. Durab. Health Monit. (1970). http://www.techscience.com/sdhm/v11n2/35277 (accessed February 26, 2022).
[3] H.-N. Li, T.-H. Yi, L. Ren, D.-S. Li, L.-S. Huo, Reviews on innovations and applications in structural health monitoring for infrastructures, Struct. Monit. Maint. 1 (2014) 1–45. https://doi.org/10.12989/SMM.2014.1.1.001.
[4] E.J. Friebele, C.G. Askins, A.B. Bosse, A.D. Kersey, H.J. Patrick, W.R. Pogue, M.A. Putnam, W.R. Simon, F.A. Tasker, W.S. Vincent, S.T. Vohra, Optical fiber sensors for spacecraft applications, Smart Mater. Struct. 8 (1999) 813–838, https://doi.org/10.1088/0964-1726/8/6/310.
[5] E. Saeter, K. Lasn, F. Nony, A.T. Echtermeyer, Embedded optical fibres for monitoring pressurization and impact of filament wound cylinders, Compos. Struct. 210 (2019) 608–617, https://doi.org/10.1016/j.compstruct.2018.11.051.
[6] Z.-C. Zhu, C.-W. Chu, H.-T. Bian, J.-C. Jiang, An integration method using distributed optical fiber sensor and Auto-Encoder based deep learning for detecting sulfurized rust self-heating of crude oil tanks, J. Loss Prev. Process Ind. 74 (2022), https://doi.org/10.1016/j.jlp.2021.104623 104623.
[7] S. Hassani, M. Mousavi, A.H. Gandomi, Structural Health Monitoring in Composite Structures: A Comprehensive Review, Sensors. 22 (2022) 153, https://doi.org/10.3390/s22010153.
[8] C. Kralovec, M. Schagerl, Review of Structural Health Monitoring Methods Regarding a Multi-Sensor Approach for Damage Assessment of Metal and Composite Structures, Sensors. 20 (2020) 826, https://doi.org/10.3390/s20030826.
[9] C.-C. Cheng, Y.-L. Lo, B.S. Pun, Y.M. Chang, W.Y. Li, An Investigation of Bonding-Layer Characteristics of Substrate-Bonded Fiber Bragg Grating, J. Light. Technol. 23 (2005) 9.
[10] M.F. Bado, J.R. Casas, A. Dey, C.G. Berrocal, Distributed Optical Fiber Sensing Bonding Techniques Performance for Embedment inside Reinforced Concrete Structures, Sensors. 20 (2020) 5788, https://doi.org/10.3390/s20205788.
[11] C. Miguel Giraldo, J. Zúñiga Sagredo, J. Sánchez Gómez, P. Corredera, Demonstration and Methodology of Structural Monitoring of Stringer Runs out Composite Areas by Embedded Optical Fiber Sensors and Connectors Integrated during Production in a Composite Plant, Sensors. 17 (2017) 1683. https://doi.org/10.3390/s17071683.
[12] M. Mulle, A. Yudhanto, G. Lubineau, R. Yaldiz, W. Schijve, N. Verghese, Internal strain assessment using FBGs in a thermoplastic composite subjected to quasi-static indentation and low-velocity impact, Compos. Struct. 215 (2019) 305–316, https://doi.org/10.1016/j.compstruct.2019.02.085.
[13] E. Voet, G. Luyckx, I. De Baere, J. Degrieck, J. Vlekken, E. Jacobs, H. Bartelt, High Strain Monitoring during Fatigue Loading of Thermoplastic Composites Using Imbedded Draw Tower Fibre Bragg Grating Sensors, Adv. Sci. Technol. 56 (2008) 441–446, https://doi.org/10.4028/www.scientific.net/AST.56.441.
[14] S. Goossens, B.D. Pauw, T. Geernaert, M.S. Salmanpour, Z.S. Khodaei, E. Karachalios, D. Saenz-Castillo, H. Thienpont, F. Berghmans, Aerospace-grade surface mounted optical fibre strain sensor for structural health monitoring on composite structures evaluated against in-flight conditions, Smart Mater. Struct. 28 (2019) 065008. https://doi.org/10.1088/1361-665X/ab1458.
[15] B. Glisic, D. Inaudi, Integration of long-gage fiber optic sensor into a fiber-reinforced composite sensing tape, in: D. Inaudi, E. Udd (Eds.), San Diego, CA, 2003 179. https://doi.org/10.1117/12.484262.
[16] K.S.C. Kuang, L. Zhang, W.J. Cantwell, I. Bennion, Process monitoring of aluminum-foam sandwich structures based on thermoplastic fibre–metal laminates using fibre Bragg gratings, Compos. Sci. Technol. 65 (2005) 669–676, https://doi.org/10.1016/j.compscitech.2004.09.005.
[17] C. Davis, M. Knowles, N. Rajic, G. Swanton, Evaluation of a Distributed Fibre Optic Strain Sensing System for Full-Scale Fatigue Testing, Procedia Struct. Integr. 2 (2016) 3784–3791, https://doi.org/10.1016/j.prostr.2016.06.471.
[18] J.V. Roosbroeck, E. Jacobs, E. Voet, J. Vlekken, Installation and test procedures of optical strain gauges for aeronautical applications, in: 20th Int. Conf. Opt. Fibre Sens., International Society for Optics and Photonics, 2009: p. 75037Q. https://doi.org/10.1117/12.837542.
[19] J. Zhang, M. de Souza, C. Creighton, R.J. Varley, New approaches to bonding thermoplastic and thermoset polymer composites, Compos. Part Appl. Sci. Manuf. 133 (2020), https://doi.org/10.1016/j.compositesa.2020.105870 105870.
[20] R.C. Don, J.W.G. Jr, S.H. McKnight, Bonding techniques for high performance thermoplastic compositions, US5643390A, 1997. https://patents.google.com/patent/US5643390A/en (accessed May 13, 2022).
[21] Surface treatment for adhesive bonding: Thermoset vs. thermoplastic composites, (n.d.). https://www.compositesworld.com/articles/surface-treatment-for-adhesive-bonding-thermoset-vs-thermoplastic-composites (accessed May 13, 2022).
[22] E.A.Y.F. Corp Henkel, Adhesives for Fiber Optics Assembly: Making the Right Choice, (n.d.). https://www.photonics.com/Articles/Adhesives_for_Fiber_Optics_Assembly_Making_the/a25147 (accessed June 24, 2021).
[23] W. Hufenbach, M. Gude, A. Czulak, M. Kretschmann, Development and implementation of an automatic integration system for fibre optic sensors in the braiding process with the objective of online-monitoring of composite structures, in: J.P. Lynch, K.-W. Wang, H. Sohn (Eds.), San Diego, California, USA, 2014 906134. https://doi.org/10.1117/12.2035613.
[24] G. Dell'Anno, I. Partridge, D. Cartié, A. Hamlyn, E. Chehura, S. James, R. Tatam, Automated manufacture of 3D reinforced aerospace composite structures, Int. J. Struct. Integr. 3 (2012) 22–40, https://doi.org/10.1108/17579861211209975.
[25] A. Yousefpour, M. Hojjati, J.-P. Immarigeon, Fusion Bonding/Welding of Thermoplastic Composites, J. Thermoplast. Compos. Mater. 17 (2004) 303–341, https://doi.org/10.1177/0892705704045187.
[26] H. Li, L. Zhu, M. Dong, X. Lou, Y. Guo, Analysis on strain transfer of surface-bonding FBG on Al 7075–T6 alloy host, Optik. 127 (2016) 1233–1236, https://doi.org/10.1016/j.ijleo.2015.10.227.
[27] A. Hehr, M. Norfolk, J. Wenning, J. Sheridan, P. Leser, P. Leser, J.A. Newman, Integrating Fiber Optic Strain Sensors into Metal Using Ultrasonic Additive Manufacturing, JOM. 70 (2018) 315–320, https://doi.org/10.1007/s11837-017-2709-8.
[28] M. Nascimento, P. Inácio, T. Paixão, E. Camacho, S. Novais, T.G. Santos, F.M.B. Fernandes, J.L. Pinto, Embedded Fiber Sensors to Monitor Temperature and Strain of Polymeric Parts Fabricated by Additive Manufacturing and Reinforced with NiTi Wires, Sensors. 20 (2020) 1122, https://doi.org/10.3390/s20041122.
[29] A. Kantaros, D. Karalekas, Fiber Bragg grating based investigation of residual strains in ABS parts fabricated by fused deposition modeling process, Mater. Des. 50 (2013) 44–50, https://doi.org/10.1016/j.matdes.2013.02.067.
[30] S.N. Economidou, D. Karalekas, Optical sensor-based measurements of thermal expansion coefficient in additive manufacturing, Polym. Test. 51 (2016) 117–121, https://doi.org/10.1016/j.polymertesting.2016.03.001.
[31] C. Kousiatza, D. Karalekas, In-situ monitoring of strain and temperature distributions during fused deposition modeling process, Mater. Des. 97 (2016) 400–406, https://doi.org/10.1016/j.matdes.2016.02.099.

[32] A.G. Leal-Junior, C. Marques, M.R.N. Ribeiro, M.J. Pontes, A. Frizera, FBG-Embedded 3-D Printed ABS Sensing Pads: The Impact of Infill Density on Sensitivity and Dynamic Range in Force Sensors, IEEE Sens. J. 18 (2018) 8381–8388, https://doi.org/10.1109/JSEN.2018.2866689.
[33] A. Leal-Junior, A. Theodosiou, C. Díaz, C. Marques, M. Pontes, K. Kalli, A. Frizera-Neto, Fiber Bragg Gratings in CYTOP Fibers Embedded in a 3D-Printed Flexible Support for Assessment of Human-Robot Interaction Forces, Materials. 11 (2018) 2305, https://doi.org/10.3390/ma11112305.
[34] N. Reggiani Manzo, G.T. Callado, C.M.B. Cordeiro, L.C.M. Vieira Jr., Embedding optical Fiber Bragg Grating (FBG) sensors in 3D printed casings, Opt. Fiber Technol. 53 (2019), https://doi.org/10.1016/j.yofte.2019.102015 102015.
[35] F. Falcetelli, R. Di Sante, E. Troiani, Strategies for Embedding Optical Fiber Sensors in Additive Manufacturing Structures, in: P. Rizzo, A. Milazzo (Eds.), Eur. Workshop Struct. Health Monit, Springer International Publishing, Cham, 2021, pp. 362–371, https://doi.org/10.1007/978-3-030-64908-1_34.
[36] R. Zou, R. Cao, M.A.S. Zaghloul, A. Yan, R. Chen, P. Ohodnicki, M. Buric, D. Crandall, X. Liang, A. To, K. Chen, Optical Fiber Sensor-Fused Additive Manufacturing and Its Applications in Residual Stress Measurements in Titanium Parts, in: Asia Pac. Opt. Sens. Conf. 2016 Pap. Th1A7, Optica Publishing Group, 2016 Th1A.7. https://doi.org/10.1364/APOS.2016.Th1A.7.
[37] S. Wang, K. Lasn, C.W. Elverum, D. Wan, A. Echtermeyer, Novel in-situ residual strain measurements in additive manufacturing specimens by using the Optical Backscatter Reflectometry, Addit. Manuf. 32 (2020) 101040.
[38] S. Wang, E. Sæter, K. Lasn, Comparison of DOFS Attachment Methods for Time-Dependent Strain Sensing, Sensors. 21 (2021) 6879, https://doi.org/10.3390/s21206879.
[39] W. Zhang, W. Chen, Y. Shu, X. Lei, X. Liu, Effects of bonding layer on the available strain measuring range of fiber Bragg gratings, Appl. Opt. 53 (2014) 885–891, https://doi.org/10.1364/AO.53.000885.
[40] S.-C. Her, C.-Y. Tsai, Strain measurement of fiber optic sensor surface bonding on host material, Trans. Nonferrous Met. Soc. China. 19 (2009) 143–149, https://doi.org/10.1016/S1003-6326(10)60262-2.
[41] H. Zhao, Q. Wang, Y. Qiu, J. Chen, Y. Wang, Z. Fan, Strain transfer of surface-bonded fiber Bragg grating sensors for airship envelope structural health monitoring, J. Zhejiang Univ. Sci. A. 13 (2012) 538–545, https://doi.org/10.1631/jzus.A1100336.
[42] J. Li, Z. Zhou, J. Ou, Interface strain transfer mechanism and error modification for adhered FBG strain sensor, in: Y.N. Kulchin, O.B. Vitrik, V.I. Stroganov (Eds.), Khabrovsk, 2005 278–287. https://doi.org/10.1117/12.634066.
[43] G. Zhou, H. Li, L. Ren, D. Li, Influencing parameters analysis of strain transfer in optic fiber Bragg grating sensors, in: N. Meyendorf, G.Y. Baaklini, B. Michel (Eds.), San Diego, CA, 2006 61790R. https://doi.org/10.1117/12.661858.
[44] S.-C. Her, C.-Y. Huang, Effect of Coating on the Strain Transfer of Optical Fiber Sensors, Sensors. 11 (2011) 6926–6941, https://doi.org/10.3390/s110706926.
[45] N. Perogamvros, P. Motwani, A. Murphy, S. Taylor, Investigation of Surface Strain Fields of Thermoplastic Composites Using Fibre Optic Sensors, In BSSM 14th International Conference on Advances in Experimental Mechanics: Friction and wear, 2019.
[46] M. Liang, N. Chen, X. Fang, G. Wu, Strain transferring mechanism analysis of the surface-bonded FBG sensor, Appl. Opt. 57 (2018) 5837, https://doi.org/10.1364/AO.57.005837.
[47] G. Xue, X. Fang, X. Hu, L. Gong, Measurement accuracy of FBG used as a surface-bonded strain sensor installed by adhesive, Appl. Opt. 57 (2018) 2939, https://doi.org/10.1364/AO.57.002939.
[48] S.-C. Her, C.-Y. Huang, The Effects of Adhesive and Bonding Length on the Strain Transfer of Optical Fiber Sensors, Appl. Sci. 6 (2016) 13, https://doi.org/10.3390/app6010013.
[49] K.S. Kumar, A.C. Reddy, Study on Reinforcement Materials for Nylon Matrix Composites - A Review, Int J Sci Eng Res 7 (2016) 156–160.
[50] F. Ning, W. Cong, J. Qiu, J. Wei, S. Wang, Additive manufacturing of carbon fiber reinforced thermoplastic composites using fused deposition modeling, Compos. Part B Eng. 80 (2015) 369–378, https://doi.org/10.1016/j.compositesb.2015.06.013.
[51] A. Barrias, J.R. Casas, S. Villalba, A Review of Distributed Optical Fiber Sensors for Civil Engineering Applications, Sensors. 16 (2016) 748, https://doi.org/10.3390/s16050748.
[52] R. Chen, Z. Peng, M. Wang, A. Yan, S. Li, S. Huang, M.-J. Li, K.P. Chen, Spatially resolved fibre cavity ring down spectroscopy, Sci. Rep. 10 (2020) 20167, https://doi.org/10.1038/s41598-020-76721-y.
[53] A. Iadicicco, D. Natale, P. Di Palma, F. Spinaci, A. Apicella, S. Campopiano, Strain Monitoring of a Composite Drag Strut in Aircraft Landing Gear by Fiber Bragg Grating Sensors, Sensors. 19 (2019) 2239, https://doi.org/10.3390/s19102239.